

HIGH-SPATIAL-RESOLUTION IMAGING COMBINING HIGH-ORDER ADAPTIVE OPTICS, FRAME SELECTION, AND SPECKLE MASKING RECONSTRUCTION

CARSTEN DENKER¹, DULCE MASCARINAS¹, YAN XU¹, WENDA CAO¹,
GUO YANG¹, HAIMIN WANG¹, PHILIP R. GOODE¹ and THOMAS RIMMELE²

¹*New Jersey Institute of Technology, Center for Solar-Terrestrial Research 323 Martin Luther King Blvd, Newark, NJ 07102*

(e-mail: cdenker@adm.njit.edu)

²*National Solar Observatory, Sacramento Peak Observatory, P.O. Box 62, Sunspot, NM 88349-0062*

(Received 7 March 2004; accepted 5 May 2004)*

Abstract. We present, for the first time, high-spatial-resolution observations combining high-order adaptive optics (AO), frame selection, and post-facto image correction via speckle masking. The data analysis is based on observations of solar active region NOAA 10486 taken with the Dunn Solar Telescope (DST) at the Sacramento Peak Observatory (SPO) of the National Solar Observatory (NSO) on 29 October 2003. The high Strehl ratio encountered in AO corrected short-exposure images provides highly improved signal-to-noise ratios leading to a superior recovery of the object's Fourier phases. This allows reliable detection of small-scale solar features near the diffraction limit of the telescope. Speckle masking imaging provides access to high-order wavefront aberrations, which predominantly originate at high atmospheric layers and are only partially corrected by the AO system. In addition, the observations provided qualitative measures of the image correction away from the lock point of the AO system. We further present a brief inspection of the underlying imaging theory discussing the limitations and prospects of this multi-faceted image reconstruction approach in terms of the recovery of spatial information, photometric accuracy, and spectroscopic applications.

1. Introduction

To advance our understanding of small-scale magnetic fields, higher light-gathering capacity and spatial resolution are essential. This has led to several initiatives for a new generation of solar telescopes with 1 m apertures and beyond. These efforts include the new Swedish 1 m Solar Telescope (SST), which is already operational (Scharmer *et al.*, 2003); the German 1.5 m GREGOR telescope (Volkmer *et al.*, 2003) and the 1.6 m New Solar Telescope (NST) at Big Bear Solar Observatory (BBSO, Goode *et al.*, 2003), which are currently under construction; and the 4 m Advanced Technology Solar Telescope (ATST) under NSO stewardship, which approaches the end of its design and development phase (Keil *et al.*, 2003).

This new or next generation of solar telescopes can only achieve its potential by relying on extensive use of *in situ* and/or post-facto image correction. Correlation tracking, spot tracking, and adaptive optics (AO) systems belong

*The editors apologize to the authors: due to a misunderstanding during the editorial process, the publication of this paper has been delayed.

into the aforementioned class, while blind deconvolution algorithms, (speckle) phase diversity techniques, speckle deconvolution, speckle holography, speckle masking method, etc. comprise the latter. The next steps in image reconstruction can be separated in two categories: (1) implementing post-facto techniques on parallel processors pushing image reconstruction toward real-time applications (e.g., Denker, Yang, and Wang, 2001) and (2) effectively combining *in situ* and post-facto image correction. An excellent example of the latter case has been presented by Scharmer *et al.* (2002), who used a *low-order* AO system with 15 corrected modes, frame selection, and an implementation of the phase diversity technique at the SST to study sunspot fine structure with a resolution of about $0.12''$. Here, however, we present a more qualitative approach based on data obtained with a *high-order* AO system, frame selection, and speckle masking imaging.

The science target of our study was solar active region NOAA 10486, which has been one of the surprises of the declining phase of solar cycle 23. NOAA 10486 and its companions NOAA 10484 and 10488, which were all naked-eye sunspot groups, were responsible for major flare activity including several X-class flares. This activity culminated in an X28 flare on 4 November, 2003, the largest X-ray flare in recorded history. The scientific results of the observing are presented by Xu *et al.* (2004). In the following sections, we present and discuss the image reconstruction procedure, where we applied “without scruples” the speckle masking method (Weigelt, 1977; Weigelt and Wirtitzer, 1983; Lohmann, Weigelt, and Wirtitzer, 1983; de Boer, 1993) to AO corrected images, before scrutinizing the underlying assumptions, limitations, and prospects in the final section “Discussion and Conclusions”.

2. Adaptive Optics

The 76 cm entrance aperture of the Dunn Solar Telescope (DST) is located about 40 m above ground to mitigate the effects of boundary layers seeing and the entire light path is evacuated until the light reaches the AO system (Rimmele, 2000; Rimmele *et al.*, 2003) at the observing room to avoid internal telescope seeing. The effective focal length of the $f/72$ system is about $f_{\text{eff}} = 55$ m. The expression “high-order AO system” is related to the number actuators N controlling the shape of the deformable mirror. To bring the residual mean square phase error below one radian requires $N_0 = 0.27(D/r_0)^2$ actuators (see Equation 2.23 in Roddier, 1999), where D is the diameter of the telescope and r_0 is the Fried-parameter, respectively. Assuming a median Fried-parameter of $r_0 = 5$ cm at Sacramento Peak Observatory (SPO), which is consistent with the ATST Site Survey Interim Report (Beckers *et al.*, 2003), the number of control parameter should exceed $N_0 = 60$ to allow full wavefront compensation. The SPO AO system is also the prototype for a twin-system at BBSO (Ren *et al.*, 2003; Didkovsky *et al.*, 2003). Both AO systems will be used in dedicated observing runs as important building blocks to develop multi-conjugate AO for solar observations.

A tip/tilt mirror precedes the AO system to preserve the dynamic range of the 77 mm diameter, 97 actuator, deformable mirror to efficiently correct the high-order wavefront aberrations. These wavefront aberrations are detected by a Shack–Hartman wavefront sensor from slope measurements derived from 76 sub-apertures, which are recorded on 200×200 pixels of a custom-built Complex Metal Oxide Semiconductor (CMOS) camera (Richards *et al.*, 2004). The data acquisition rate is 2.5 kHz. The closed loop bandwidth of the system is about 130 Hz (0 dB crossover). The high order AO system has achieved Strehl ratios in excess of 0.7 (Langlois, Rimmele, and Moretto, 2004).

The maximum field of view (FOV) for science observations of the AO system is about $180'' \times 180''$. The AO corrected data were acquired in two distinct science channels: (1) near-infrared (NIR) filtergrams at $\lambda = 1,560 \pm 5$ nm were obtained with a high-speed (30 frames s^{-1}), large-format (1024×1024 pixel, FOV: $91'' \times 91''$), low-noise ($>60\%$ quantum efficiency, 14-bit digitization, >70 dB dynamic range) HgCdTe/Al₂O₃ CMOS camera based on a TCM 8600 sensor manufactured by Rockwell Scientific Imaging and (2) broad-band, short-exposure images “specklegrams” were obtained in the green continuum. These science data will be presented in a separate paper (Xu *et al.*, 2004).

3. Frame Selection

The 4 ms short-exposure images were obtained with a 1024×1024 pixel 1M15 CCD camera manufactured by Dalsa. This high-speed, large-format CCD camera is usually used with the real-time image reconstruction (RTIR) system at BBSO (Denker, Yang, and Wang, 2001), which can reconstruct 1024×1024 pixel images at a 1-minute cadence. However, during this observing run at the DST, the images were digitized as 12-bit integers, saved on hard-disk, and later archived on DLT tape for post-processing.

The FOV of the speckle interferometry channel was $81'' \times 81''$, which corresponds to an image scale of $0.08'' \text{ pixel}^{-1}$. The observations were taken in a green continuum window at 520 nm and the bandpass of the interference filter was 52 nm. The diffraction limited resolution of the 76 cm DST at 527 nm is defined according to the Rayleigh criterion $\theta_{\text{Rayleigh}} = 1.22\lambda/D = 0.17''$. However, the Rayleigh criterion is related to the separation of two point sources. Therefore, we prefer the criterion $\theta = \lambda/D = 0.14''$, which is appropriate when dealing with extended objects and telescopes with circular apertures. Comparing the diffraction limit and image scale indicates that the speckle images are slightly undersampled by about 12%. In order to obtain more reliable information at high spatial frequencies, i.e., to improve the signal-to-noise ratio at these frequencies, the data should have been oversampled by at least 50%. However, this would have restricted the FOV too much for our science program. This choice is also reflected in the average power spectra shown in Figure 4, where we conservatively applied a noise filter suppressing

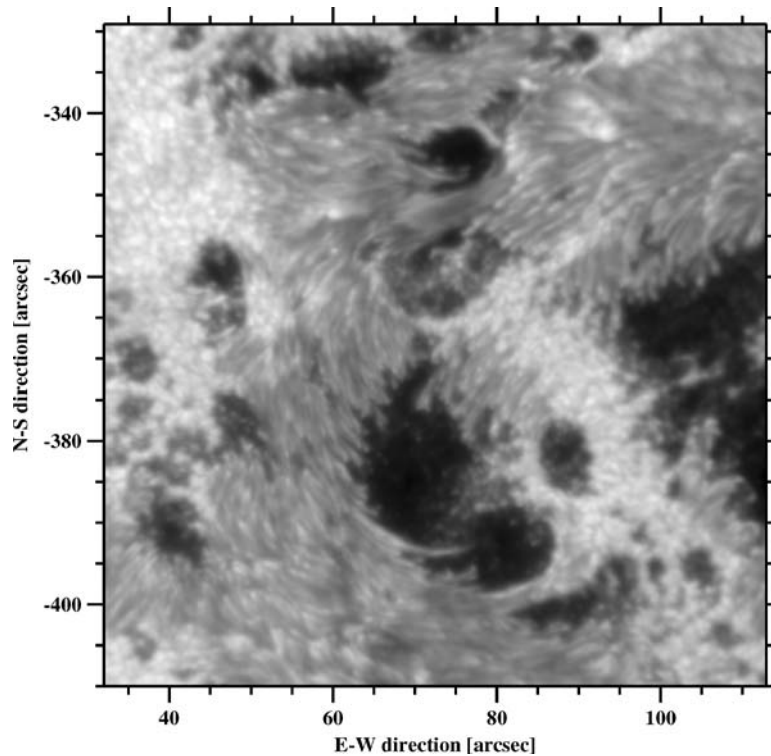


Figure 1. Solar active region NOAA 10486 observed at 16:48 UT on 29 October, 2003. The “long-exposure” image is the average of 100 short-exposure images captured during a period of about 15 s, which corresponds to an equivalent exposure time of 400 ms – an exposure time that is typically encountered in high-resolution two-dimensional spectroscopy.

Fourier amplitudes at high spatial frequencies ($f/f_{\text{nyq}} > 0.75$), i.e., at the intersection of the speckle reconstruction and short-exposure image power spectra.

A total of 102 sequences of short-exposure images were taken with a 1-min cadence from 15:28 to 17:28 UT, with the exception of a short interruption in the data acquisition from 16:09 to 16:27 UT. Each sequence consists of a series of 100 short-exposure images, which were selected from a total of 200 images. The frame selection algorithm is based on the rms-contrast of a distinct solar feature (e.g., Scharmer, 1989), which was in this case a small region of granulation in the north-east corner of the FOV (see Figures 1–4 for details). The images were acquired at a rate of 15 frames s^{-1} . The first 100 frames are just stored in a stack of 100 pre-allocated memory buffers and the 100 subsequent frames overwrite the images with the lowest rms-contrast only if their rms-contrast is higher. This has the advantage of requiring the smallest amount of memory and overhead for keeping track of rms-contrast values. Since the granulation area used to compute the image contrast was small, the camera operated close to its nominal data acquisition rate, so that individual image sequences were obtained within about 15 s. Saving the

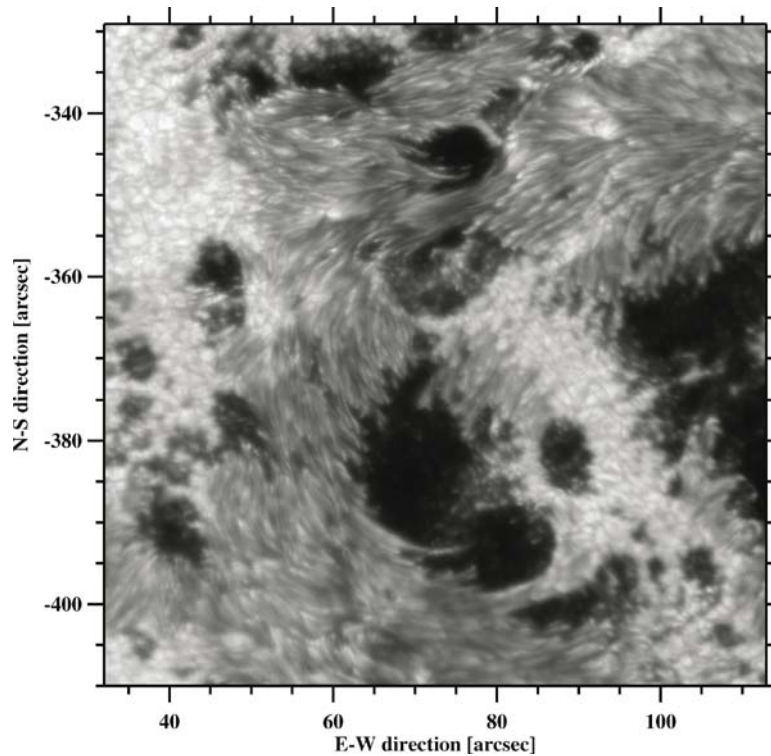


Figure 2. The short-exposure “reference” image, which is used in the image reconstruction process to compute image motion and differential image motion, is a frame selected image with the highest granular rms-contrast out of a total of 200 short-exposure images.

data to hard disk took another 15 s and the next sequence was started after pausing 30 s. This slower data acquisition rate was a compromise between our scientific objectives and the limited amount of hard disk space, a situation that has been alleviated by the real-time image reconstruction system at BBSO (Denker, Yang, and Wang, 2001).

4. Image Reconstruction

Speckle masking imaging requires a sequence of short-exposure images each of which is sufficient to “freeze” the wavefront aberrations, which makes it possible to separate the object information and the information on atmospheric turbulence. The exposure time of the specklegrams was 4 ms. The first steps in preprocessing the data concern the usual corrections by means of the average dark and flat field image. The image displacement within the sequence is removed with respect to the image with the highest rms-contrast. Since the short-exposure images were obtained with

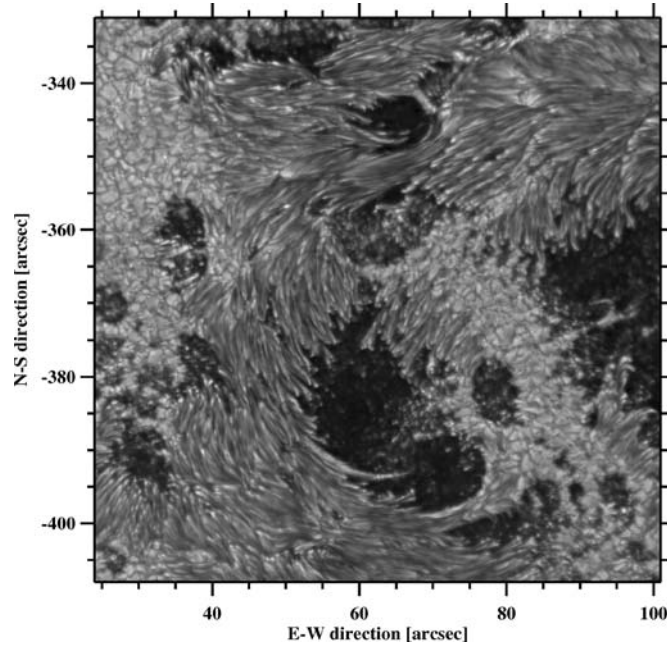


Figure 3. Image reconstruction of solar active region NOAA 10486 after AO correction, frame selection, and speckle masking technique have been applied.

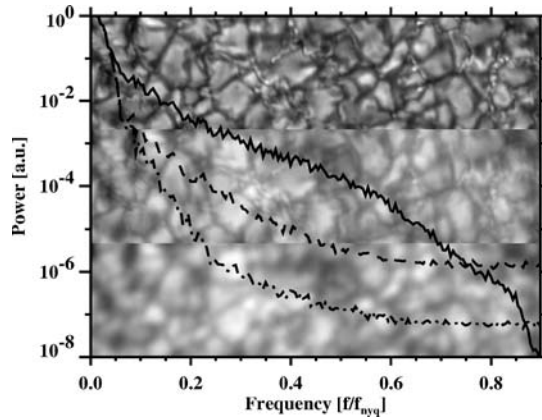


Figure 4. Average power spectra of solar granulation have been obtained from 90 individual, one-dimensional, $28.5''$ -long intensity profiles for the speckle reconstruction (*solid line*), short-exposure image (*dashed line*), and long-exposure image (*dashed-dotted line*), respectively. The spatial frequencies on the abscissa have been normalized with respect to the Nyquist frequency f_{Nyq} and the power values are given in arbitrary units normalized to the first order Fourier component. The three background panels show from top to bottom the same area of granulation in the speckle reconstruction, the short-exposure image, and the long-exposure image. The panels were extracted from the north-east corner of Figures 1–3, respectively, and have been rotated counter-clockwise by 90° to fit the aspect ratio of the plotting window. The panels have been independently scaled between maximum and minimum brightness, thus, contrasts are not directly comparable.

an AO system, the average image motion should be small and negligible. This was confirmed by computing the average image motion by means of a cross-correlation analysis with a result of $0.013''$. Because this result was of the same order as the inherent errors of the cross-correlation algorithm, it is essentially zero. Since speckle interferometry is only valid for a small region, the isoplanatic patch, the specklegrams have to be divided into mosaics of partially overlapping images. Each subimage has a size of approximately $5.1'' \times 5.1''$. The differential image displacement in these stacks of 64×64 pixel images is also removed.

The time interval between consecutive sequences was approximately 1 min, which is sufficient to study the evolution of solar fine structures with local correlation tracking. Detailed studies of fine structure, however, will require higher temporal resolution. The typical lifetime of photospheric fine structures is in the range of 5 to 10 min. The other important time scale for speckle imaging is given by the fact that the object should not change while we take a sequence of short-exposure images. A typical value for photospheric proper motions is about 2 km s^{-1} . In 60 s, a feature could move 120 km or $0.17''$, which is about the size of the resolution element $\theta = \lambda/D = 0.14''$. Therefore, the data had to be acquired within about 30 s.

The intensity distribution in the focal plane of a telescope, $i(\vec{x})$, is given by the convolution of the intensity distribution of the object, $i_0(\vec{x})$, and the point spread function (PSF) $s(\vec{x})$, which describes the atmospheric turbulence along the line of sight:

$$i(\vec{x}) = i_0(\vec{x})s(\vec{x}). \quad (1)$$

Fourier transformation of Equation (1) yields

$$I(\vec{q}) = I_0(\vec{q})S(\vec{q}), \quad (2)$$

where the upper case letters denote the Fourier transformation and \vec{q} is a two-dimensional, normalized spatial frequency. We use the spectral ratio technique to derive the Fried parameter r_0 (von der Lühne, 1984). Roughly, the Fried parameter corresponds to the aperture of the largest telescope that would just be diffraction limited. The spectral ratio is given by

$$\mathcal{E}(\vec{q}) = \frac{|\langle I(\vec{q}) \rangle|^2}{\langle |I(\vec{q})|^2 \rangle} = \frac{|\langle I_0(\vec{q}) \rangle|^2}{\langle |I_0(\vec{q})|^2 \rangle} \frac{|\langle S(\vec{q}) \rangle|^2}{\langle |S(\vec{q})|^2 \rangle} = \frac{|\langle S(\vec{q}) \rangle|^2}{\langle |S(\vec{q})|^2 \rangle}, \quad (3)$$

where $\langle \dots \rangle$ denotes an ensemble average. Equation 3 is independent of the object's intensity distribution and it is only a function of the two average transfer functions $|\langle S(\vec{q}) \rangle|^2$ and $\langle |S(\vec{q})|^2 \rangle$, which in turn are just functions of the Fried parameter. $\langle |S(\vec{q})|^2 \rangle$ is the so called speckle transfer function (STF). To measure the Fried parameter, the observed spectral ratios are then compared with tabulated theoretical values of the STF (Korff, 1973) and the average short-exposure modulation transfer function (MTF, Fried, 1966). The amplitudes of the object's Fourier transform were

corrected according to the classical method of Labeyrie (1970):

$$|I_0(\vec{q})|^2 = \frac{\langle |I(\vec{q})|^2 \rangle}{\langle |S(\vec{q})|^2 \rangle}. \quad (4)$$

To derive the phases of the object's Fourier transform, we use the speckle masking method (Weigelt, 1977; Weigelt and Wirtitzer, 1983; Lohmann, Weigelt, and Wirtitzer, 1983; de Boer, 1993),

$$\langle I^3(\vec{q}, \vec{p}) \rangle = I_0^3(\vec{q}, \vec{p}) \langle S^3(\vec{q}, \vec{p}) \rangle, \quad (5)$$

where $I^3(\vec{q}, \vec{p}) = I(\vec{q})I(\vec{p})I^*(\vec{q} + \vec{p})$ is the speckle masking bispectrum and $*$ denotes a conjugate complex quantity, $\langle S^3(\vec{q}, \vec{p}) \rangle$ is the average speckle masking transfer function (SMTF). A detailed description of the technical aspects of the phase reconstruction algorithm is given by Pehlemann and von der Lühe (1989). The central obscuration of the DST was taken into account in computing the SMTF. However, since the radius of the obscuration is only 10% of the aperture radius, its effect on the STF is negligible. A sensitive noise filter (de Boer, 1996) is applied during the calculation of these phases. Back-transformation of the modulus and phases of the object's Fourier transform yields a mosaic of partially overlapping speckle reconstructions. Finally, we align these reconstructions very accurately and assemble the mosaic of subimages.

5. Results

Figures 1–3 illustrate the image quality that can be achieved by combining AO, frame selection, and speckle masking imaging. Figure 1 is the “long-exposure” image, i.e., the average of 100 short-exposure images corresponding to an effective exposure time of about 400 ms. Exposure times in the range from 100 ms to several seconds are typically encountered in high-resolution two-dimensional spectro-polarimetry, an application where AO systems outperform post-processing techniques, since the latter rely on short exposure times ($\ll 40$ ms, i.e., the typical correlation time scale of daytime seeing) to freeze wavefront aberrations. An example of a “short-exposure” image is the frame selected image obtained with an exposure time of 4 ms shown in Figure 2. This “reference” image is used in the image reconstruction procedure to remove image motion and differential image motion. Imaging applications are the domain of post-processing techniques, as can be seen in the improved spatial resolution and contrast of the speckle reconstructed image in Figure 3.

In order to obtain a more quantitative measure of image quality, a region of granulation with 90×360 pixel corresponding to $7.1'' \times 28.5''$ was selected to compute contrasts and power spectra. Note that this region, which is shown as the background image of the power spectra plot in Figure 4, is in the vicinity of the sunspot. It contains filigree and magnetic knots, thus, caution should be taken when comparing contrast and power spectra to quiet-Sun values. The granular contrasts of

the speckle reconstruction, the short-exposure image, and the long-exposure image were 9.3, 5.1 and 4.4%, respectively. The granulation was observed at a heliocentric angle of $\mu = \cos \theta \approx 0.9$ and our contrast values are relatively low compared to other speckle reconstructed observations, e.g., Wilken *et al.* (1997) report granular rms-contrasts, which decrease monotonically from 13.5% at disc center to about 8–9% at $\mu = 0.1$. The contrast of the speckle reconstruction strongly depends on the proper choice of the STF, which in turn is derived with the spectral ratio technique. However, the underlying imaging theory of the spectral ratio technique (Fried, 1966; Korff, 1973) is not applicable to AO corrected images, since both the short- and long-exposure transfer functions consist of a diffraction-limited core on top of a seeing halo (see Figure 3.3 in Roddier, 1999). The granular contrast of 9.3% was derived with a STF for a Fried parameter of $r_0 = 15.6$ cm. Choosing a STF for $r_0 = 11.9$ cm yields a contrast of 13.1% consistent with Wilken *et al.* (1997). Obviously, we need to find a better way to determine the STF for AO corrected speckle images. We will use the seeing cut-off frequency determined from the spectral ratio technique in the following discussion, since it has a more fundamental meaning than the specific meaning of the Fried parameter. In principle, the ratio of the diffraction-limited core to the seeing halo as well as the Strehl ratio should be encoded in the seeing cut-off frequency. However, we are still in the process of developing the underlying theory to extract this information.

The power spectra are averages derived from 90 individual one-dimensional intensity profiles of solar granulation. In Figure 4 and all subsequent plots in the Fourier domain, all frequencies are given in terms of the Nyquist frequency $f_{\text{nyq}} \approx 9.6 \text{ Mm}^{-1}$, which was derived from the diffraction limit $\theta = \lambda/D = 0.14''$. Zero-order terms, which correspond to the image mean, are usually omitted. Since all images have a finite size, the lowest frequency in all plots corresponds to image gradients, which has been normalized to unity. The power spectra in Figure 4 are represented by a solid line for the speckle reconstruction, by a dashed line for the short-exposure image, and by a dashed-dotted line for the long-exposure image. The short-exposure power spectrum is basically a scaled version of the long-exposure power spectrum with consistently higher power at all frequencies. The power spectrum of the speckle reconstruction shows systematically higher power values up to a frequency $f/f_{\text{nyq}} \approx 0.75$, where it drops below the power spectrum of the short-exposure image. This is a direct result of the optimum and noise filters (de Boer, 1996) that have been conservatively applied in the reconstruction process.

In Figure 5, we show the spectral ratios (see Equation 3) that were computed for each subimage ordered by its distance from the lock point of the AO system. Two black contour lines at $\mathcal{E}(\vec{q}) = [0.5, 0.3]$ were added, showing a trend that the seeing cut-off frequency decreases with distance from the lock point. Figure 6 provides a graphical representation of the spatial distribution of the measured seeing cut-off frequencies f_c/f_{nyq} as determined from the spectral ratios for each of the 30×30 subimages across the FOV. The seeing cut-off frequencies were determined from a linear fit to the spectral ratios, where $\mathcal{E}(\vec{q}) > 0.15$, and its intercept with

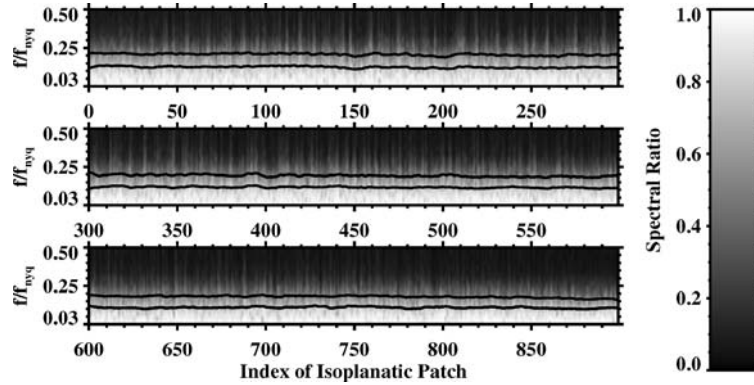


Figure 5. Each speckle reconstruction consists of a mosaic of $30 \times 30 = 900$ individually reconstructed subimages. The azimuthal averages of the spectral ratios are plotted for each subimage according to its distance from the AO lock point (see Figure 6). Two *black contour lines* at the levels $\mathcal{E}(\bar{q}) = [0.5, 0.3]$ (see Equation 3) were added for clarity.

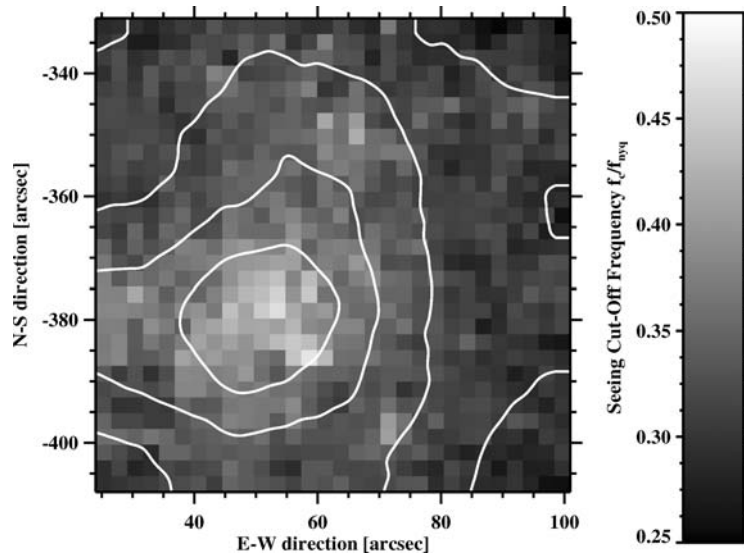


Figure 6. The seeing cut-off frequency f_c/f_{nyq} for each subimage encoded as a gray scale map. Only the approximate locations of the boxes representing the frequencies are shown, since each reconstructed subimage has an overlap of 32 pixels. The *white contour lines* were derived from a smoothed frequency map and correspond to f_c/f_{nyq} -values of 0.300, 0.325, 0.350, and 0.375, respectively. The lock point of the AO system is approximately located at heliographic coordinates $52''$ west and $380''$ south.

the frequency axis. The overall range of the frequencies ranges from about 0.25 at the periphery of the FOV to 0.50 near the AO lock point with an average value $\bar{f}_c/f_{nyq} = 0.33$. The contour lines in Figure 6 were computed from a smoothed image, where we applied a Lee filter algorithm (Lee, 1986) with a nine pixel wide

sampling window. The coordinates of the lock point are $52''$ west and $380''$ south in heliographic coordinates and were determined by fitting the maximum of the smoothed two-dimensional frequency map. The core of the frequency map has a roughly circular shape, which fades into a cross-shaped pattern at the periphery of the FOV. This pattern is not an artifact of the smoothing operation but an inherent feature of the AO system. Finally, the seeing cut-off frequency seems to decrease linearly with increasing distance from the AO lock point.

6. Discussion and Conclusions

The region of the essential speckle masking signal is proportional to $\alpha^4 = (r_0/D)^4$ and depends on two distinct and separate terms related to seeing (α^4) and telescope (see Equation 24 and its derivation in von der L uhe, 1985),

$$\langle S^3(\vec{q}, \vec{p}) \rangle = \langle S(\vec{q})S(\vec{p})S^*(\vec{q} + \vec{p}) \rangle \cong 0.356\alpha^4 S_0(\vec{q}, \vec{p}), \quad (6)$$

where $S_0(\vec{q}, \vec{p})$ depends only on the complex amplitude transmittance of the telescope's entrance pupil. In this region, the SMTF provides unbiased information on the object phases and does not introduce systematic phase terms. The improved Strehl ratio due to the AO system helps the phase recovery, since in this case the signal-to-noise ratio is more important than the signal itself, which is proportional to α^4 , and could be rather low. The approximations used to derive Equation (6) are only valid in a limited range of spatial frequencies ($\alpha < |\vec{q}|$, $|\vec{p}|$, and $|\vec{q} - \vec{p}| < (1 - \alpha)$), i.e., the region of the essential speckle masking signal, but become more accurate with deteriorating seeing or with increasing telescope apertures, i.e., speckle masking imaging becomes an even more important post-processing technique in the context of the 4 m aperture ATST. Since the Fried parameter r_0 is proportional to $\lambda^{6/5}$, about a factor of four between 500 nm and 1.56 μm , α can become large for NIR observations, thus, limiting the range of spatial frequencies. A practical limit for the speckle masking technique is $\alpha = r_0/D > 0.3$.

In principle, speckle masking is able to remove telescope aberrations on scales larger than the Fried parameter r_0 . However, the AO system already removes telescope aberrations, which can be distinguished from atmospheric seeing, since they usually occur at low temporal frequencies as can be determined from temporal power spectra of Zernike modes representing the wavefront fluctuations (see Figure 5 in Rimmele, 2000). Even in well-designed telescopes, telescope aberrations cannot be neglected, e.g., the entrance windows of vacuum telescopes have been identified as a significant source of wavefront aberrations. In any case, the AO system ensures that the effects of atmospheric seeing surmount the telescope aberrations, thus, supporting even stronger the assumptions inherent to the derivation of Equation 6. As far as the recovery of Fourier phases is concerned, AO correction of telescope aberrations actually enforces the underlying theory of speckle masking.

According to Moore's law of exponential growth in computing power, we can expect an increase of computing power by a factor of 16 over the next 6 years, which will allow us to operate 2048×2048 pixel or even larger format CCD cameras for speckle interferometry. This will be right in time for the next generation of 2 to 4 m-class telescopes, which will provide diffraction limited observations with a spatial resolution of better than $0.05''$ at 500 nm with a FOV of about $100'' \times 100''$, sufficiently large to cover sunspots and substantial parts of active regions. The data acquisition rate for such a system is expected to be in excess of one GByte per minute. We are certain that large format, high frame rate CCD cameras for speckle interferometry or other post-processing techniques in combination with parallel computers will become standard post-focus instruments for advanced solar telescopes. Real-time image reconstruction (Denker, Yang, and Wang, 2001) will not only aid our basic scientific understanding of solar activity but also enhance space weather forecast and prediction capabilities. The visualization of photospheric flow fields in solar active regions with the highest possible spatial and temporal resolution is extremely important in predicting solar flares, filament eruptions and disappearances, as well as coronal mass ejections (CMEs).

Finally, we would like to highlight with Figure 7 some of the science that will be addressed in upcoming papers. Xu *et al.* (2004) present high-resolution observations

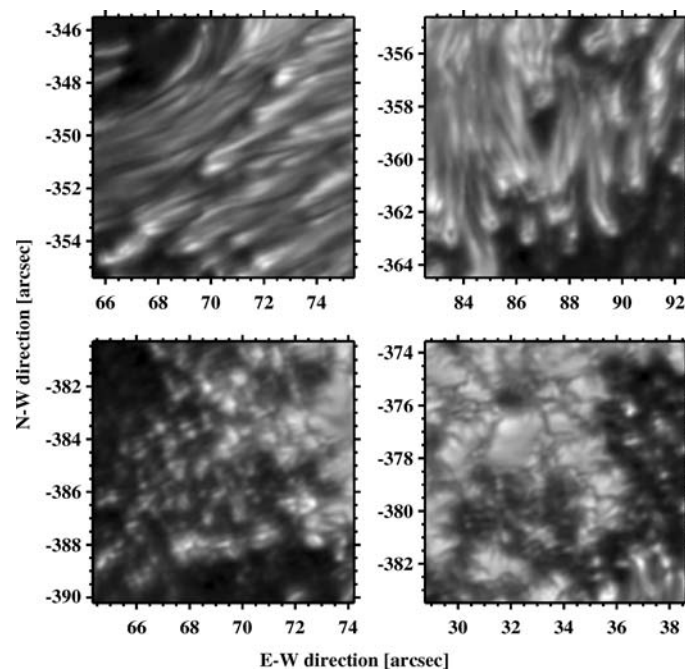


Figure 7. Detailed views of small-scale features shown in Figure 3: *top-left*: dark cores inside penumbral filaments, *top-right*: internal dark structures in penumbral grains, *bottom-left*: densely packed umbral dots, and *bottom-right*: magnetic knots, filigree, and pores.

of an NIR X10 white-light flare. We will use the speckle reconstructed time series to study changes in the pre-flare state of active region NOAA 10486 and search for flow patterns that are related to the strong magnetic shear observed in NOAA 10486. The top row shows two features, dark cores inside umbral filaments and internal dark structures in penumbral grains, which were first reported by Scharmer *et al.* (2002). Since our multi-faceted image reconstruction approach is quite different, we are certain that these features are real. The bottom row of Figure 7 shows a region of densely packed umbral dots, which exhibit a striking similarity to magnetic knots, filigree, and pores observed near the eastern edge of the speckle reconstruction.

Acknowledgements

This work was supported by NSF under grant ATM 00-86999, ATM 02-36945, IIS ITR 03-24816 and AST MRI 00-79482 and by NASA under grant NAG 5-12782. Dulce Mascarinas has been supported through a summer research for undergraduates stipend of the New Jersey Space Grant Consortium. We would like to thank Drs. Franz Kneer and Claus-Rüdiger de Boer (Universitäts-Sternwarte Göttingen) for providing the original version of the IDL speckle masking algorithms. Obtaining the excellent data would not have been possible without the help of the dedicated observing staff at the Dunn Solar Telescope. The National Solar Observatory/Sacramento Peak is a Division of the National Optical Astronomy Observatories, which is operated by the Association of Universities for Research in Astronomy, Inc., under cooperative agreement with the National Science Foundation. We thank the referee, Mats Löfdahl, for constructive comments that led to a substantial improvement of the paper.

References

- Beckers, J., Brandt, P., Collados, M., Denker, C., Hill, F., Kuhn, J., and Ständer, K.: 2003, *ATST Proj. Doc.* **16**, Tucson, Arizona.
- de Boer, C. R.: 1993, Ph.D. Thesis, Georg-August Universität Göttingen, Germany.
- de Boer, C. R.: 1996, *Astron. Astrophys. Suppl. Ser.* **120**, 195.
- Denker, C., Yang, G., and Wang, H.: 2001, *Solar Phys.* **202**, 63.
- Didkovsky, L. V., Dolgushyn, A., Marquette, W. H., Nenow, J., Varsik, J., Goode, P. R., Hegwer, S. L., Ren, D., Fletcher, S., Richards, K., Rimmele, T., Denker, C., and Wang, H.: 2003, *Proc. SPIE* **4853**, 630.
- Fried, D. L.: 1966, *J. Opt. Soc. Am.* **56**, 1372.
- Goode, P. R., Denker, C., Didkovsky, L. I., Kuhn, J. R., and Wang, H.: 2003, *J. Korean Astron. Soc.* **36**, 125.
- Keil, S. L., Rimmele, T., Keller, C. U., Hill, F., Radick, R. R., Oschmann, J. M., Warner, M., Dalrymple, N. E., Briggs, J., Hegwer, S. L., and Ren, D.: 2003, *Proc. SPIE* **4853**, 240.
- Korff, D.: 1973, *J. Opt. Soc. Am.* **63**, 971.
- Labeyrie, A.: 1970, *Astron. Astrophys.* **6**, 85.
- Langlois, M., Rimmele, T. R., and Moretto, G.: 2004, *Proc. SPIE* **5171**, 187.
- Lee, J.-S.: 1986, *Opt. Eng.* **25(5)**, 636.

- Lohmann, A. W., Weigelt, G. P., and Wirtzner, B.: 1983, *Appl. Opt.* **22**, 4028.
- Pehlemann, E. and von der Lühse, O.: 1989, *Astron. Astrophys.* **216**, 333.
- Ren, D., Hegwer, S., Rimmele, T., Didkovsky, L., and Goode, P. R.: 2003, *Proc. SPIE* **4853**, 593.
- Richards, K., Rimmele, T. R., Hill, R., and Chen, J.: 2004, *Proc. SPIE* **5171**, 316.
- Rimmele, T.: 2000, *Proc. SPIE* **4007**, 218.
- Rimmele, T. R., Richards, K., Hegwer, S. L., Ren, D., Fletcher, S., Gregory, S., Didkovsky, L. V., Denker, C., Marquette, W., Marino, J., and Goode, P. R.: 2003, *Proc. SPIE* **4839**, 635.
- Roddier, F.: 1999, *Adaptive Optics in Astronomy*, Cambridge University Press.
- Scharmer, G. B.: 1989, *NATO ASI Ser.* **263**, 161.
- Scharmer, G. B., Gudiksen, B. V., Kiselman, D., Löfdahl, M. G., and Rouppe van der Voort, L. H. M.: 2002, *Nature* **420**, 151.
- Scharmer, G. B., Bjelksjö, K., Korhonen, T. K., Lindberg, B., and Petterson, B.: 2003, *Proc. SPIE* **4853**, 341.
- Volkmer, R., von der Lühse, O., Kneer, F., Staude, J., Hofmann, A., Schmidt, W., Sobotka, M., Soltau, D., Wiehr, E., Wittmann, A., and Berkefeld, T.: 2003, *Proc. SPIE* **4853**, 360.
- von der Lühse, O.: 1984, *J. Opt. Soc. Am. A* **1**, 510.
- von der Lühse, O.: 1985, *Astron. Astrophys.* **150**, 229.
- Weigelt, G. P.: 1977, *Opt. Comm.* **21**, 55.
- Weigelt, G. and Wirtzner, B.: 1983, *Opt. Lett.* **8**, 389.
- Wilken, V., de Boer, C. R., Denker, C., and Kneer, F.: 1997, *Astron. Astrophys.* **325**, 819.
- Xu, Y., Cao, W., Liu, C., Yang, G., Jing, J., Denker, C., and Wang, H.: 2004, *Astrophys. J. Lett.* **607**, L131.